

# Synthetic seismic anisotropy models within a slab impinging on the core–mantle boundary

Sanne Cottaar,<sup>1,2</sup> Mingming Li,<sup>3</sup> Allen K. McNamara,<sup>3</sup> Barbara Romanowicz<sup>1,4,5</sup> and Hans-Rudolf Wenk<sup>1</sup>

<sup>1</sup>Department of Earth and Planetary Science, UC Berkeley, Berkeley CA 94720, USA. E-mail: sc845@cam.ac.uk

<sup>2</sup>now at, Pembroke College and University of Cambridge, Cambridge, UK

<sup>3</sup>School of Earth and Space Exploration, Arizona State University, Tempe, AZ 85287, USA

<sup>4</sup>Collège de France, Paris, France

<sup>5</sup>Institut de Physique du Globe, Paris, France

Accepted 2014 June 24. Received 2014 June 19; in original form 2014 February 19

## SUMMARY

The lowermost few hundreds of kilometres of the Earth's mantle are elastically anisotropic; seismic velocities vary with direction of propagation and polarization. Observations of strong seismic anisotropy correlate with regions where subducted slab material is expected. In this study, we evaluate the hypothesis that crystal preferred orientation (CPO) in a slab, as it impinges on the core–mantle boundary, is the cause of the observed anisotropy. Next, we determine if fast polarization directions seen by shear waves can be mapped to directions of geodynamic flow. This approach is similar to our previous study performed for a 2-D geodynamic model. In this study, we employ a 3-D geodynamic model with temperature-dependent viscosity and kinematic velocity boundary conditions defined at the surface of the Earth to create a broad downwelling slab. Tracers track the deformation that we assume to be accommodated by dislocation creep. We evaluate the models for the presence of perovskite or post-perovskite and for different main slip systems along which dislocation creep may occur in post-perovskite [(100),(010) and (001)]—resulting in four different mineralogical models of CPO. Combining the crystal pole orientations with single crystal elastic constants results in seismically distinguishable models of seismic anisotropy. The models are evaluated against published seismic observations by analysing different anisotropic components: the radial anisotropy, the splitting for (sub-)vertical phases (i.e. azimuthal anisotropy), and the splitting for subhorizontal phases. The patterns in radial anisotropy confirm our earlier results in 2-D. Observations of radial anisotropy and splitting in subhorizontal phases are mostly consistent with our models of post-perovskite with (010)-slip and (001)-slip. Our model of (001)-slip predicts stronger splitting than for (010)-slip for horizontally propagating phases in all directions. The strongest seismic anisotropy in this model occurs where the slab impinges on the core–mantle boundary. The azimuthal anisotropy pattern for (001)-slip shows fast axis directions at the edges of the slab (sub-)parallel to flow directions, suggesting horizontal flows may be mapped out in the lowermost mantle using seismic observations.

**Key words:** Plasticity, diffusion, and creep; Composition of the mantle; Body waves; Seismic anisotropy; Rheology: mantle.

## 1 INTRODUCTION

In the upper mantle, observations of seismic anisotropy in the Earth reflect deformation due to present day dynamics (e.g. Becker *et al.* 2008; Long & Becker 2010). While the bulk of the lower mantle appears seismically isotropic, the presence of strong and laterally varying seismic anisotropy in the lowermost 200–300 km, the D'' layer, is now well established. The cause of this anisotropy as well as

its relation to geodynamics remains a topic of much research (e.g. Kendall & Silver 1998; Nowacki *et al.* 2011; Wenk *et al.* 2011).

Different types of shear body wave observations provide evidence for the presence of seismic anisotropy in D''. Vinnik *et al.* (1989) made the first observation of differential SH–SV velocities in  $S_{\text{diff}}$ , where the SV component was delayed with respect to SH by several seconds. Other localized observations of  $S_{\text{diff}}$  splitting followed (Lay & Young 1991), with many in regions where the

velocity in D'' is faster than average (e.g. Kendall & Silver 1996; Matzel *et al.* 1996; Garnero & Lay 1997; Cottaar & Romanowicz 2013). Splitting is also found in ScS (e.g. Lay & Helmberger 1983; Russell *et al.* 1998; Rokosky *et al.* 2006; Nowacki *et al.* 2013) and in direct S (e.g. Ford *et al.* 2006). Core phases, SKS and SKKS, show differential splitting and can be used to map strong lateral variations in azimuthal anisotropy (Niu & Perez 2004; Restivo & Helffrich 2006; Wang & Wen 2007; Long 2009; He & Long 2011; Lynner & Long 2012, 2014). Additionally, variations in observed polarity of reflected waves from within the D'' layer (PdP, SdS) can be an indication of anisotropy (Thomas *et al.* 2011).

On a global scale, radial anisotropy (or transverse isotropy) has been included in whole mantle global shear velocity tomography. In some of these models (Panning & Romanowicz 2006; Kustowski *et al.* 2008) D'' stands out as a region where the lateral variations correlate with the isotropic velocity structure in D''; with  $V_{SH} > V_{SV}$  in fast regions, and patches of  $V_{SV} > V_{SH}$  near the large low shear velocity provinces (LLSVPs) beneath the Pacific and Africa. More recent global models show a more variable signature in fast regions (Panning *et al.* 2010; Chang *et al.* 2014). Normal modes confirm the global nature of radial P-wave anisotropy and find a probable global signature of  $V_{PV} > V_{PH}$  (Beghein *et al.* 2006), but constraining lateral variation of radial P-wave anisotropy remains difficult. A study using body waves (Boschi & Dziewonski 2000; Soldati *et al.* 2003) shows no clear signature in fast regions at the base of the mantle, and because of large trade-offs with core structure this model must first be independently confirmed.

Seismologists face several challenges in characterizing anisotropy in the lowermost mantle. One of them is to obtain good azimuthal coverage as well as the vertically propagating core phases for a given location that are needed to constrain the full elastic tensor. Another challenge is to correct for contamination from near-source and near-receiver anisotropy in the upper mantle. In order to eliminate upper mantle effects on the source side, one approach is to study deep earthquakes. However, large and deep earthquakes are few and their global distribution is limited to mainly South America and the western Pacific. In recent studies, direct S phases are used to correct for the contamination of the source- and receiver side anisotropy in ScS phases, providing more opportunities to find crossing rays and measure tilted radial anisotropy (Wookey & Kendall 2008; Nowacki *et al.* 2010, 2011).

Although there is general consensus that seismic anisotropy at the base of the mantle could be associated with mantle deformation, many important questions remain on how to link the anisotropy and the flow—how to map one into the other. If the process of dislocation creep accommodates mantle deformation, it is expected to produce seismic anisotropy due to the alignment of intrinsically anisotropic minerals, that is crystal preferred orientation (CPO; e.g. Karato 1998a,b; Lay *et al.* 1998; Kendall 2000). This process is assumed to occur for olivine in the upper mantle (e.g. Dawson & Wenk 2000; Karato *et al.* 2008; Long & Becker 2010). An alternative explanation, not further considered in this study, is shape-preferred orientation (SPO) caused by alignment of melt inclusions or laminated solid materials (e.g. Kendall & Silver 1996; Hall *et al.* 2004).

When investigating the cause of anisotropy, the possible presence of post-perovskite, discovered a decade ago (Murakami *et al.* 2004; Oganov & Ono 2004), must be considered. In relatively cold regions of the D'' layer, perovskite could transform to post-perovskite, and account for the observed D'' discontinuity as well as for the faster velocities (Iitaka *et al.* 2004; Tsuchiya *et al.* 2004; Stackhouse *et al.* 2005; Wentzcovitch *et al.* 2006). In the warmer regions, the D''

transition of perovskite to post-perovskite occurs at pressures below the core–mantle boundary, explaining the absence of substantial anisotropy in some areas [e.g. beneath the Atlantic, Garnero *et al.* (2004)], and an  $V_{SV} > V_{SH}$  signature of radial anisotropy in others (Kawai & Geller 2010; Dobson *et al.* 2013). Recently, experiments have shown that the occurrence of the post-perovskite transition at mantle pressures depends not only on temperature, but also on composition (Catalli *et al.* 2009; Grocholski *et al.* 2012).

The presence of post-perovskite is argued to explain observed patterns in shear wave anisotropy, although it remains under debate which dominant slip system in post-perovskite correlates best with the observations. Different conclusions emerge when correlating global models (Walker *et al.* 2011), interpreting only fast shear velocity regions (Wenk *et al.* 2011) or focusing on local splitting observations (Nowacki *et al.* 2010, 2013). Our aim here is to evaluate synthetic anisotropy qualitatively against the range of published seismic observations to constrain what microscopic processes may be at play. We restrict our interpretation to cold regions with fast shear velocities, where the presence of cold subduction and therefore post-perovskite are more likely (Grocholski *et al.* 2012). These are also the regions where strong radial anisotropy has been observed, and many local observations of shear wave splitting have been made. We also assess the possibility of mapping vertical and horizontal flows in the lowermost mantle on the basis of these models.

In this paper, we perform forward modelling of CPO anisotropy in a subducting slab combining tools and observations developed by geodynamicists, seismologists, mineral physicists and material scientists. We developed a step-by-step approach that we previously applied to a 2-D geodynamic model (Wenk *et al.* 2011):

- (i) A geodynamic model provides characteristic information on the macroscopic strain of a slab impinging on the core–mantle boundary.
- (ii) This strain history is fed into a numerical model of mineralogical texture development within a polyphase aggregate.
- (iii) With the input of single crystal elastic constants, elastic tensors based on these aggregates are calculated for a dense sampling along the tracers,
- (iv) Finally, we compare the obtained macroscopical 3-D elastic anisotropy to published seismic observations.

These steps are described in more detail in Section 2. In Section 3, we present the results in terms of radial anisotropy, in order to relate them to the results of the 2-D geodynamic model (Wenk *et al.* 2011) and to global tomographic models. We also present the results in terms of shear wave splitting patterns, to compare them with local seismic observations. In Section 4, we compare the results to published seismological observations and other recent studies with a comparable setup (Walker *et al.* 2011; Nowacki *et al.* 2013). The resulting signatures of transverse isotropy in this study are consistent with those we found for a 2-D geodynamic model (Wenk *et al.* 2011). We find that the seismic observations agree well with post-perovskite with dominant (001)-slip; agree somewhat with post-perovskite with dominant (010)-slip; and disagree with models of perovskite and post-perovskite with (100)-slip. The successful model of post-perovskite with (001)-slip also suggests it is possible to recognize regions of strong vertical flow and map out directions of horizontal flow.

## 2 METHODS

### 2.1 Geodynamic model

As slabs subduct to the deep mantle, large-strain deformation occurs (McNamara *et al.* 2002; Wenk *et al.* 2011). In this study, the convection-induced deformation within subducted slabs is calculated in a 3D regional spherical geodynamic model. The following non-dimensional equations for conservation of mass, momentum, and energy are solved using our modified version of code CitcomCU (Zhong 2006) under Boussinesq approximation.

$$\nabla \cdot \vec{u} = 0 \quad (1)$$

$$-\nabla P + \nabla \cdot (\eta \bar{\dot{\epsilon}}) = Ra T \hat{r} \quad (2)$$

$$\frac{\partial T}{\partial t} + (\vec{u} \cdot \nabla) T = \nabla^2 T + H. \quad (3)$$

Here,  $\vec{u}$  is velocity,  $P$  is dynamic pressure,  $\eta$  is viscosity,  $\bar{\dot{\epsilon}}$  is strain rate tensor,  $Ra$  is Rayleigh number,  $T$  is temperature,  $\hat{r}$  is unit vector in vertical direction,  $t$  is time and  $H$  is internal heating. In our modified version of CitcomCU, we calculate the velocity gradient at every time step and we add passive tracers to track the velocity gradient. We also use imposed velocity surface boundary condition to simulate surface plate motion.

The domain of our 3-D regional spherical model covers  $\sqrt{3}/4$  volume of the whole spherical shell. The longitude of our model ranges from  $-90^\circ$  to  $90^\circ$ ; the colatitude ranges from  $30^\circ$  to  $150^\circ$  (Fig. 1). The model contains 384, 256 and 128 elements in longitude, colatitude, and radial directions, respectively. All boundaries have free-slip velocity boundary conditions, except for the surface in which a southward constant angular velocity of  $4 \text{ cm yr}^{-1}$  is employed in region from  $-40^\circ$  to  $40^\circ$  longitude and  $30^\circ$ – $90^\circ$  colatitude (Fig. 1). Other regions on the surface are fixed and have zero velocity. The imposed velocity boundary condition enables slabs to subduct along the equator (colatitude is  $90^\circ$ ). Temperature boundary conditions are isothermal on the top and bottom, and insulating on the sides.

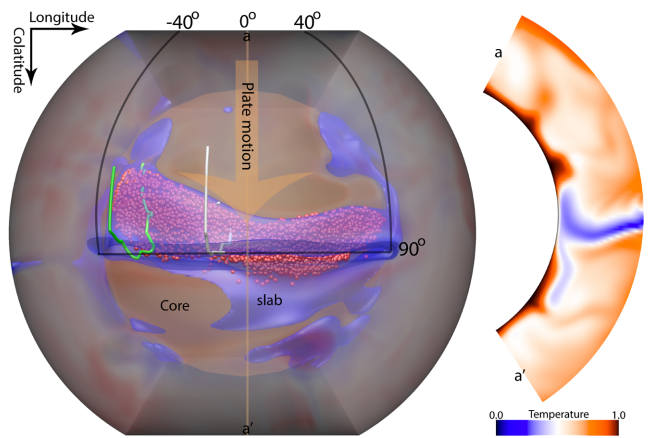


**Figure 1.** Numerical modelling of a subducting slab (blue isosurface) with tracers (red spheres) tracking the deformation within it. Only tracers that arrive at the lowermost mantle (300 km above CMB) are shown here. The white and green tubes show two paths from surface to the lowermost mantle. The background is temperature field. The core is shown in orange. Black lines outline the region with a constant angular velocity (arrow) of  $4 \text{ cm yr}^{-1}$  from north to south. Temperature cross-section at longitude of  $0^\circ$  is shown in the right panel. The snapshot is shown at 100 Myr.

The model is heated from below and internally, with a non-dimensional internal heating rate of  $H = 60$ . We employ a Rayleigh number of  $Ra = 10^8$ . Viscosity is both depth and temperature dependent. A  $30 \times$  viscosity increase is introduced at the boundary from upper mantle to lower mantle. The temperature dependent part of viscosity is expressed as  $\eta_T = \exp[A(0.6 - T)]$ , where  $T$  is non-dimensional temperature, and we use a non-dimensional activation coefficient of  $A = 9.21$ , leading to a  $10\,000 \times$  viscosity range due to changes in temperature. To generate an appropriate initial condition, we first perform a lower-resolution calculation ( $192 \times 128 \times 64$  elements) until the model comes to thermal equilibrium. Then we interpolate the temperature field to higher resolution ( $384 \times 256 \times 128$  elements) and let the calculation run for about 70 Myr to ensure the model again comes to thermal equilibrium under the new mesh. After that, 10 000 Lagrangian tracers are put on the surface of the model and later these tracers are subducted into the deep mantle with slabs. Tracers are advected using a second-order Runge–Kutta method. Velocity gradients are calculated and stored for all tracers at every time step. Fig. 1 shows a snapshot (at 100 Myr) revealing a subducted slab impinging on the core–mantle boundary, and 3371 tracers (red sphere) in subducting regions of the lowermost mantle. The deformation of the subducted slabs in the lowermost mantle, which are sampled by these tracers, are used to calculate the mineralogical texture of polyphase aggregates, as is described in the next section. In our models we use the integrated deformation along the tracers from just beneath the mantle transition zone at 700 km depth downwards.

### 2.2 Mineral physics

#### 2.2.1 Viscoplastic self-consistent modelling

For development of CPO or texture in the slab, we assume all deformation is accommodated by slip, that is the propagation of dislocations. Other deformation mechanisms, such as diffusion creep, that is the propagation of vacancies through a lattice, are not considered here.

The relative activity of different slip systems—the combination of a crystallographic plane and a propagation direction—which leads to a particular CPO, are computed with the Viscoplastic Self-Consistent (VPSC) method (Molinari *et al.* 1987; Lebensohn & Tomé 1993; Lebensohn *et al.* 2007). The texture of the sample is defined by individual crystal orientations. Here we start with 500 grains that are randomly oriented. All crystals are then viscoplastically deformed to a degree dependent on the orientation of their preferred slip systems relative to the strain. A combination of active slip systems is needed to allow for homogeneous deformation. Some are more easily activated than others as given by their relative critical resolved shear stresses (Table 1). Each crystal is treated as a finite inclusion within and interacting with a so-called infinite ‘effective medium’. The inclusion is assumed to be under constant strain. This formalism is also known as an ‘Eshelby inclusion’ (Eshelby 1957). The crystal reorientation within this medium is a result of deformation by slip along specific lattice planes and resulting rotation. The properties of the effective medium are not known in advance, but are required to fit the constitutive equations between stress and strain after averaging over all the single crystals. VPSC iterates between fitting the behaviour of the individual grains, and a consistent mean response of the effective medium on the polycrystal level, to find the self-consistent solution.

**Table 1.** Slip systems  $\{hkl\} <uvw>$  and critical resolved shear stress coefficients as used in VPSC for the different phases. We assume the cross values remain constant with pressure and temperature.

Periclase <sup>a</sup>	$\{111\}<10\bar{1}>$ 0.75	$\{110\}<\bar{1}10>$ 0.5	$\{100\}<011>$ 1				
Perovskite <sup>b</sup>	(100)[010] 3	(100)<011> 4	(010)[100] 3	(010)<101> 4	(001)[100] 1	(001)[010] 1	(001)<110> 1
Post-perovskite	(100)[010]	(100)[001]	(010)[100]	(010)[001]	(001)[100]	(001)[010]	(110)< $\bar{1}10>$ (110)[001]
A <sup>c</sup>	1	2.0	3	3	3	3	1.5 2
B <sup>d</sup>	3	3	1	1.5	3	3	3 4
C <sup>e</sup>	2	2	4	4	1	1.5	3 4

<sup>a</sup>Merkel *et al.* (2002). <sup>b</sup>Wenk *et al.* (2004). <sup>c</sup>Merkel *et al.* (2006). <sup>d</sup>Miyagi *et al.* (2009). <sup>e</sup>Miyagi *et al.* (2010).

The grain inclusions are initialized with a spheroidal shape, but become ellipsoidal under deformation of a grain. We stop further deformation when an ellipsoidal ratio of 3:1 is reached, but still allow for rotation of crystallographic planes.

To model deformation of the different phases, the VPSC method requires input on the assumed critical resolved shear stresses for the slip systems in each phase. Next the macroscopic elastic properties are determined by averaging the single crystal properties over the different orientations. The input of slip systems and elastic properties are described in the following two sections for periclase, perovskite and post-perovskite.

### 2.2.2 Deformation mechanisms

Our knowledge of slip systems for lower mantle minerals comes from experiments and first principle calculations at high pressures and temperatures. Ideally slip systems are identified by observing dislocations with a transmission electron microscope. Post-perovskite crystals, however, cannot be recovered to ambient pressure and therefore *in situ* observation of CPO development by X-ray diffraction at high pressure with diamond anvil cells (DAC) are applied. Slip systems are inferred by comparing experimental CPOs with textures obtained by VPSC simulations, assuming different slip system activities. Such experiments have been applied to periclase (Stretton *et al.* 2001; Merkel *et al.* 2002; Yamazaki & Karato 2002; Long *et al.* 2006; Lin *et al.* 2009), perovskite (Karato *et al.* 1995; Wenk *et al.* 2004) and post-perovskite (Merkel *et al.* 2006, 2007; Miyagi *et al.* 2009; Miyajima & Walte 2009; Walte *et al.* 2009; Hirose *et al.* 2010; Miyagi *et al.* 2010; Okada *et al.* 2010; Nisr *et al.* 2012).

Slip systems can also be identified by performing first principle calculations based on the Peierls–Nabarro model (e.g. Devincre *et al.* 2001; Walker *et al.* 2010). These have also been applied to periclase (Carrez *et al.* 2009), perovskite (Cordier *et al.* 2004; Mainprice *et al.* 2008), and post-perovskite (Oganov *et al.* 2005; Carrez *et al.* 2007; Metsue *et al.* 2009).

Active slip systems for periclase are on  $\{111\}$ ,  $\{110\}$  and  $\{100\}$  planes with  $\{110\}<110>$  being most active in experiments (Merkel *et al.* 2002). Calculations by Carrez *et al.* (2009) show that the  $\{100\}$  planes become more active at higher pressures. For orthorhombic perovskite, slip dominates on the  $(001)$  plane, but also occurs on  $(100)$  and  $(010)$  planes (Wenk *et al.* 2004). Calculations show  $(100)[010]$  as the most active slip system across all pressures (Mainprice *et al.* 2008). While the exact behavior of slip systems in periclase remains uncertain, our choice is not crucial for our results.

The preferred system for dislocation creep in post-perovskite is more ambiguous: Merkel *et al.* (2006) suggest that a combination of the planes  $(100)$  and  $(110)$  dominate; Miyagi *et al.* (2009) suggest  $(010)$ ; while Miyagi *et al.* (2010) suggest  $(001)<100>$  and  $(001)<010>$ . The former two experiments were done on analogue material and measurements might have been obscured by the occurring phase transition (Walte *et al.* 2009; Miyagi *et al.* 2011). In this study, however, we consider all three possibilities and characterize the resulting CPO. The slip systems for the three cases and their critical resolved shear stress values used in this study are listed in Table 1. We denote the three post-perovskite cases by the plane in the dominant slip system as follows;  $(100)$ –pPv A,  $(010)$ –pPv B and  $(001)$ –pPv C.

In our VPSC calculations a combination of many slip systems is active in each crystal. For perovskite, for example, the  $(001)$ -slip accommodates 60–70 per cent of the deformation within that phase, while for pPv C this is only  $\sim 30$  per cent. Examples of activities of the various slip systems along a tracer can be found in Wenk *et al.* (2011, fig. 6).

In our models, we assume a two-phase deformation with compositions of 75 per cent perovskite or post-perovskite with 25 per cent periclase. As can be seen from the relative critical resolved shear stress coefficients, periclase is a weaker phase and therefore tends to accommodate 35–40 per cent of the deformation in our models. If that is actually the case for a polyphase mixture remains unknown. If the periclase is only present as inclusions surrounded by perovskite, the stronger perovskite grains will be connected and accommodate most of the deformation. The exact behaviour will likely change with the amount of periclase present. VPSC calculations do not account for grain–grain interactions as each grain is treated as an individual inclusion.

The VPSC calculations for all models start with randomly oriented grains at 700 km depth. While post-perovskite is not stable in most of the lower mantle, it is a simplification in our modelling to have this phase accumulate CPO from this depth and no phase transition is included. However, the results will show that very little anisotropy develops until the lowermost mantle is reached.

### 2.2.3 Elastic constants

The other main mineralogical input consists in specifying the single crystal elastic constants for the different phases. Once the orientation distributions are calculated, the elastic constants are averaged over their orientations to obtain the overall polycrystal elastic properties. At the moment, the mineral physical experiments

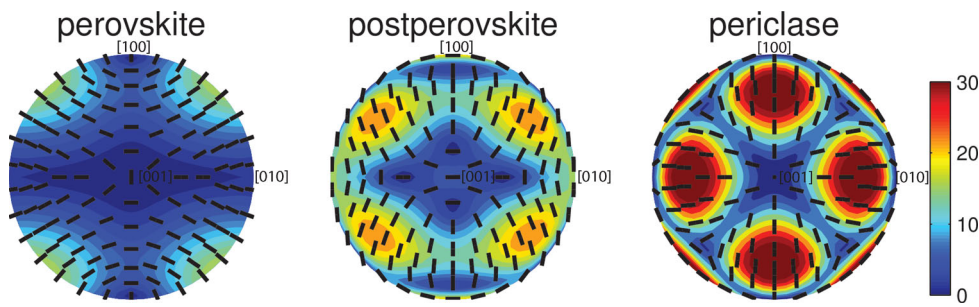


**Figure 2.** Shear wave splitting in the single crystal elastic constants at 125 GPa and 3000 K (see Table 2). Colour shows percent difference between the fast and slow shear wave velocity and the black bars indicate the polarization of the fast shear velocity. Plot is made with MSAT (Walker & Wookey 2012).

**Table 2.** Density ( $\text{g cm}^{-3}$ ) and elastic stiffness coefficients  $C_{IJ}$  (GPa) at 125 GPa and 3000 K for periclase (Karki *et al.* 2000), perovskite (Wentzcovitch *et al.* 2004), post-perovskite (Stackhouse *et al.* 2005).

	$\rho$ ( $\text{kg m}^{-3}$ )	$C_{11}$ (GPa)	$C_{12}$ (GPa)	$C_{13}$ (GPa)	$C_{22}$ (GPa)	$C_{23}$ (GPa)	$C_{33}$ (GPa)	$C_{44}$ (GPa)	$C_{55}$ (GPa)	$C_{66}$ (GPa)
Periclase	5.07	1154.0	265.5	265.5	1154.0	265.5	1154.0	198.0	198.0	198.0
Perovskite	5.25	860.0	535.5	437.0	1067.5	467.5	1053.0	294.0	249.5	284.5
Post-perovskite	5.35	1220.0	474.0	359.0	899.0	493.0	1176.0	273.0	245.0	376.0

are not capable of measuring single crystal elastic properties under lower mantle conditions of pressure and temperature. Here we rely on values that are obtained by computational methods for atomic and molecular structure using basic laws of quantum mechanics, a.k.a. *ab initio* calculations.

We apply the elastic constants for periclase from Karki *et al.* (2000), for perovskite from Wentzcovitch *et al.* (2004) and for post-perovskite from Stackhouse *et al.* (2005). Fig. 2 shows the differential shear wave velocity and polarization direction; Table 2 gives an overview of all the applied constants. Post-perovskite is intrinsically more anisotropic than perovskite. In our previous 2-D study, we also applied the elastic constants obtained from first-principles computations with the quasi-harmonic approximation from Wentzcovitch *et al.* (2006) and compared the results with those obtained using elastic constants from Stackhouse *et al.* (2005) (see fig. 10 of Wenk *et al.* 2011). As the elastic constants of Stackhouse *et al.* (2005) show stronger intrinsic anisotropy, they result in stronger anisotropy patterns. The resulting signature of radial anisotropy was mostly consistent for both sets of elastic constants (only the shear wave anisotropy for the pPv B model switched sign). A comparison in methods and results between these two ab-initio studies is given in Stackhouse & Brodholt (2007) and Wentzcovitch (2010).

We apply the elastic constants at constant pressure and temperature of 125 GPa and 3000 K, respectively. Varying the elastic constants with pressure and temperature would strongly affect the absolute isotropic velocity variations, but not the anisotropic patterns, and we do not aim to fit the absolute isotropic velocities here.

### 2.3 Comparing with seismological results

We evaluate the resulting anisotropic patterns in the lowermost 300 km of the slab, where deformation is strong due to impinging on the core–mantle boundary. Our model results in over 150 000 full elastic tensors within the slab. While the tensors do represent different times in the geodynamic model, we will treat the result as a snap-shot model that can be directly compared to seismological observations. In general the tracers show similar development in anisotropy, with the larger variations being towards the edges of the slab.

Examples of shear wave splitting in the elastic tensors are shown along four tracers in Fig. 3. It is difficult to analyse these results; we will therefore summarize different components of anisotropy in the slab to compare to seismic observations.

To evaluate the anisotropy for phases in any given direction ( $\mathbf{x}$ ) in an elastic tensor, one computes the Christoffel matrix (Babuska & Cara 1991). The Christoffel matrix,  $\gamma_{kl}$ , is the matrix of squared velocities for all polarizations in that specific direction:

$$\gamma_{kl} = C_{ijkl}x_i x_j / \rho, \quad (4)$$

where  $\rho$  is the density. The eigenvalues of the matrix give the squared phase velocities,  $V_p^2$ ,  $V_{S1}^2$  and  $V_{S2}^2$  and the eigenvectors are the corresponding polarization directions. We apply the implementation in the Matlab Seismic Anisotropy Toolkit (Walker & Wookey 2012). We will specifically compare the splitting in mostly horizontally propagating phases, such as S and ScS, and splitting in mostly vertically propagating phases, such as SKS and SKKS (Section 3.1). The strength of splitting is defined as 100 per cent  $\frac{2(V_{S1} - V_{S2})}{V_{S1} + V_{S2}}$ . A shear wave that propagates for 200 km in the lowermost mantle through 4 per cent anisotropy accumulates  $\sim 1.2$  s of splitting.

However, we first compare our results with the strong component of radial anisotropy in the lowermost mantle as seen in global tomographic models. Radial anisotropy represents the difference in velocity between horizontally and vertically polarized shear waves which are propagating horizontally, defined as  $\xi = V_{SH}^2 / V_{SV}^2$ , and the difference between horizontally and vertically propagating P waves, defined as  $\phi = V_{PV}^2 / V_{PH}^2$  (Montagner & Nataf 1986).

For this comparison, we compute the components of radial anisotropy in our models. For a given location, the shear wave radial anisotropy,  $\xi$ , is obtained by averaging  $V_{SH}$  and  $V_{SV}$  over all horizontally propagation directions. For (6x6) elastic tensor in the Voigt notation, C, with coordinates (long., colat., rad.) this leads to the following expression (Browaeys & Chevrot 2004):

$$\xi = \frac{V_{SH}^2}{V_{SV}^2} = \frac{1/8(C_{11} + C_{22}) - 1/4C_{12} + 1/2C_{66}}{1/2(C_{55} + C_{44})}. \quad (5)$$

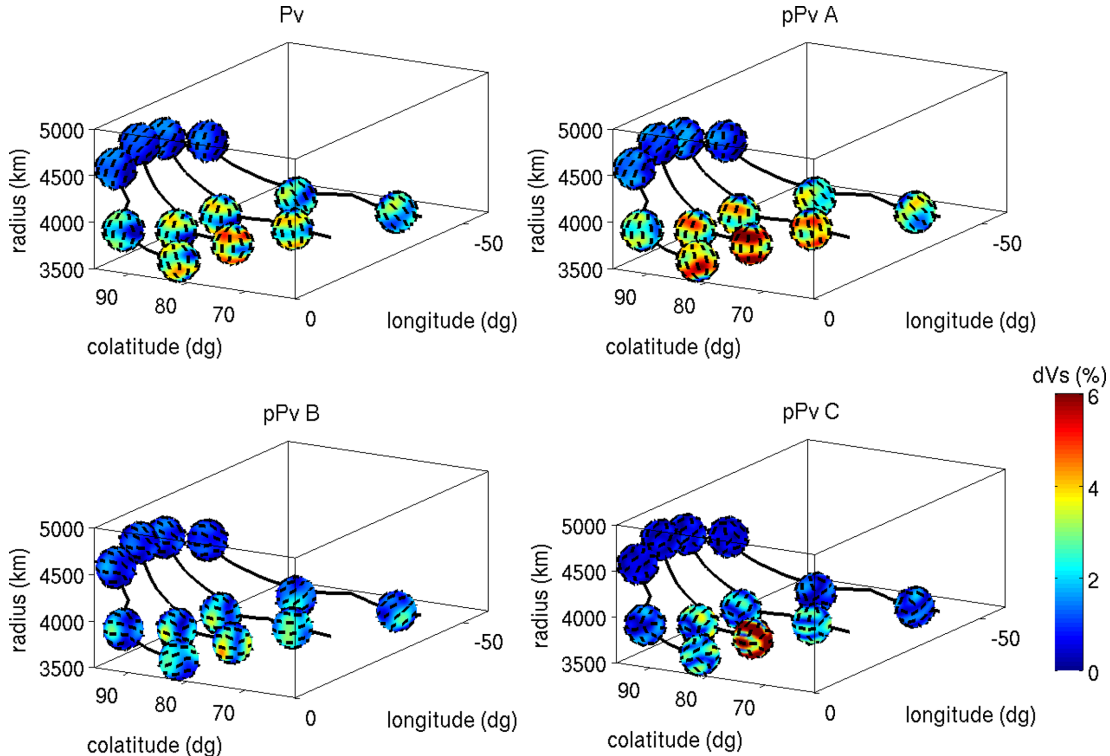


**Figure 3.** For several locations along four tracers shear wave splitting strength is shown as a function of propagation up to 6 per cent (red). The black bars indicate the polarization direction of the fast axis.

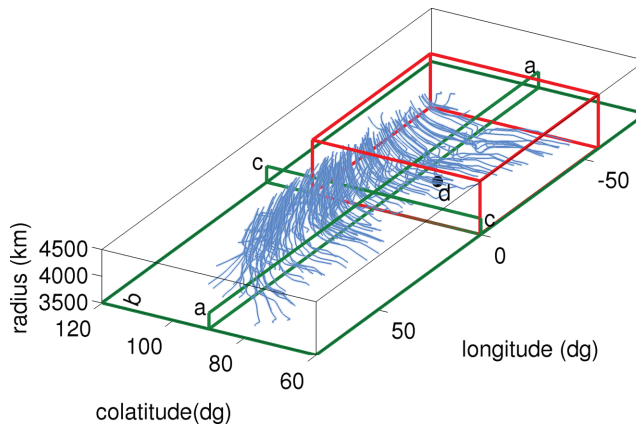


**Figure 4.** Geometry of the various plots. Tracers are plotted in blue. Only a subset of the tracers is plotted so individual tracers can be distinguished as flow lines. Red box shows the section plotted in Figs 5 and 6. In green are the two vertical slices a. and c. and the horizontal slice b. as shown in Figs 7 to 10. The dot denoted with d. is the location of panel (d).

For the expression of radial anisotropy,  $\phi$ ,  $V_{PH}$  is averaged over all horizontal directions:

$$\phi = \frac{V_{PV}^2}{V_{PH}^2} = \frac{C_{33}}{3/8(C_{11} + C_{22}) + 1/4C_{12} + 1/2C_{66}} . \quad (6)$$

The results of this analysis are presented in Section 3.1. To aid the understanding of the various boxes and cross-sections plotted in the following sections, Fig. 4 shows a subset of the tracers to outline the slab and the various geometries of the plots.

A more thorough method to compare these models to observations, would be to forward model body waves through our models

and then invert for the anisotropic structure. This, however, is computationally beyond the scope of this study.

### 3 RESULTS

#### 3.1 Radial anisotropy

Figs 5 and 6 show the radial anisotropic components in a quarter of the slab domain (see Fig. 4). The different assemblages result in opposite signatures of radial shear wave anisotropy; the pPv B and C models correspond with seismic observations of  $V_{SH} > V_{SV}$  (blue), while the Pv and pPv A models have an opposite signature (red). The patterns are consistent across most of the slab, with the exception of rotated patterns at the short ends of the slab. The strongest radial anisotropy is located where the slab impinges on the core–mantle boundary, this localization is strongest in the pPv C model.

The global models of Panning & Romanowicz (2006) and Kustowski *et al.* (2008) show  $V_{SH} > V_{SV}$  beneath subducting slabs, while the models of Panning *et al.* (2010) and Chang *et al.* (2014) show more varying signature in the ring around the Pacific. The signature of  $V_{SH} > V_{SV}$  agree best with local observations (e.g. Vinnik *et al.* 1989; Garnero & Lay 1997; Nowacki *et al.* 2013).  $V_{SH} > V_{SV}$  agrees with the pPv B and pPv C models. Knowledge of  $P$ -wave anisotropy beneath slabs could further constrain the different dominant slip systems as it has an opposite signature for these two models.

The signs of radial anisotropy agree with those of our 2-D model (see fig. 10 of Wenk *et al.* 2011). The location of the strongest radial anisotropy, however, appears different; while the strongest anisotropy in our 3-D model appears right below the subducting slab, in our 2-D model the stronger anisotropy develops after the slab changes direction as it encounters the core–mantle boundary.

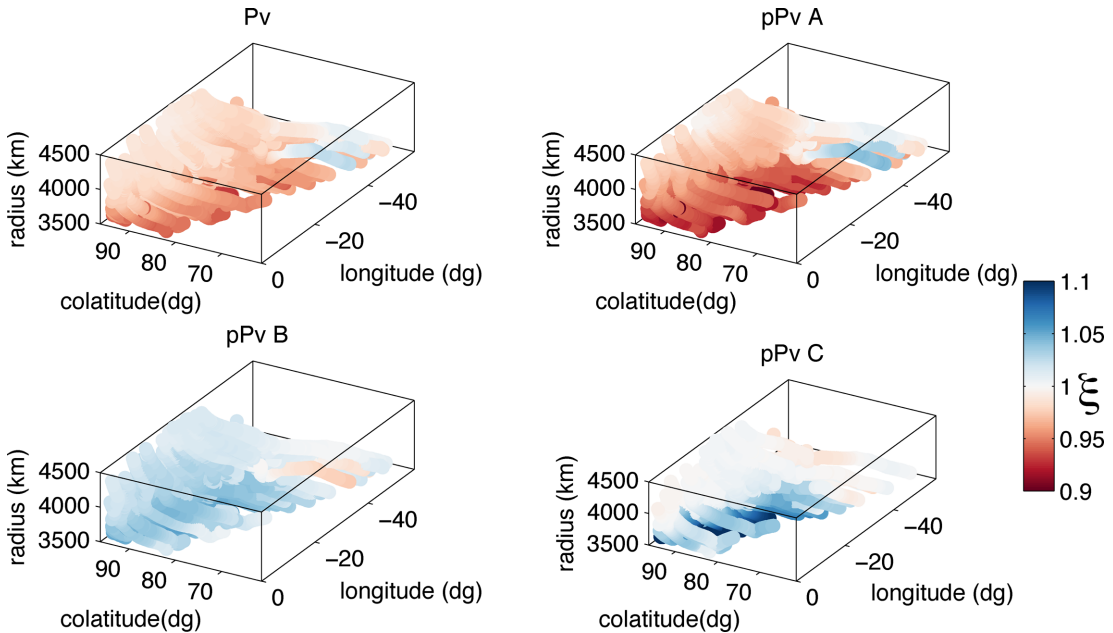


**Figure 5.** Radial anisotropy for  $S$  waves ( $\xi$ ) shown in the northerwestern part of the slab (Fig. 4).

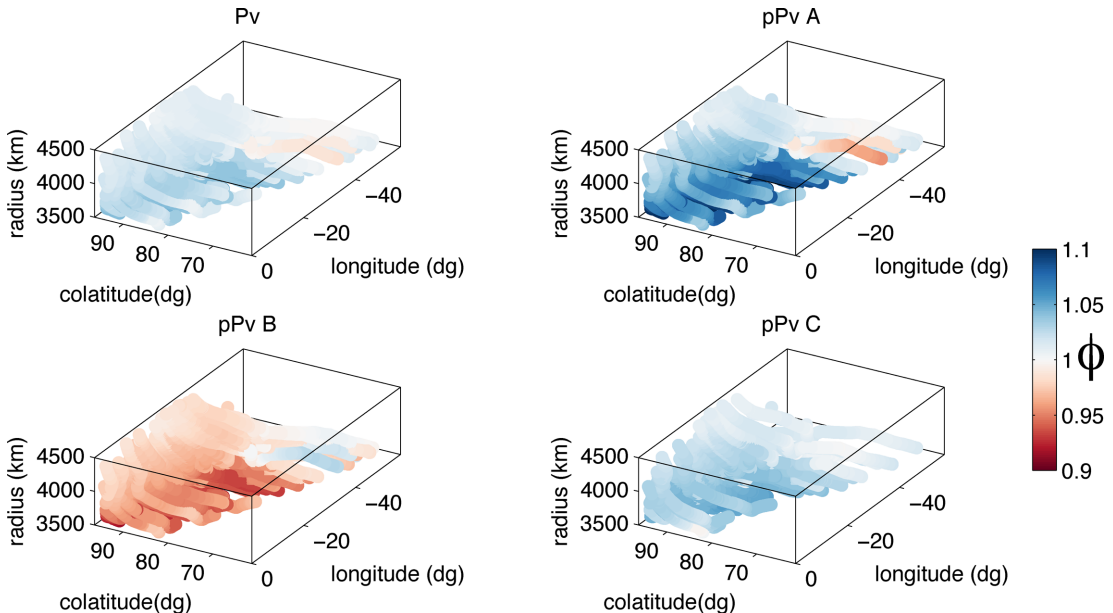


**Figure 6.** Radial anisotropy for  $P$  waves ( $\phi$ ) shown in the northerwestern part of the slab (Fig. 4).

### 3.2 Shear wave splitting

Local observations of shear wave splitting constrain more complex anisotropy including strong lateral variations. Our model suggests the presence of strong shear wave splitting beneath the slabs. Figs 7–10 show shear wave splitting strengths and fast axes in three slices in orthogonal directions across the slab (subplots a–c) and a pole projection of the splitting as a function of propagation direction for one location (subplot d). The percentage of splitting refers to the percent difference between the fast and slow polarized shear waves.

Note that for all models the shear wave splitting of horizontally propagating waves is stronger than those of vertically propagating ones. While the radial anisotropy and splitting in horizontal directions are strong at the centre of the slab, where the slab impinges on

the CMB, the azimuthal anisotropy or vertical splitting increases in strength at the edges, where the flow rotates to horizontal. Overall, the splitting is most significant in the pPv C model; the weakest splitting is seen in model pPv B. Although the anisotropy in model pPv B could still produce measurable splitting for long paths, we will later discuss the reasons why our models are probably overpredicting the splitting amplitudes.

The Pv model is the only model that shows strong azimuthal splitting in the centre of the slab (Fig. 7b). There, the fast axis direction is slab-parallel (i.e. parallel to the length of the slab). The general fast axis direction rotates at the edges to close-to-parallel to the horizontal flow directions. Models pPv A and C show similar strong azimuthal splitting towards the edges of the slab with fast axis directions (sub-)parallel to flow. All three of these

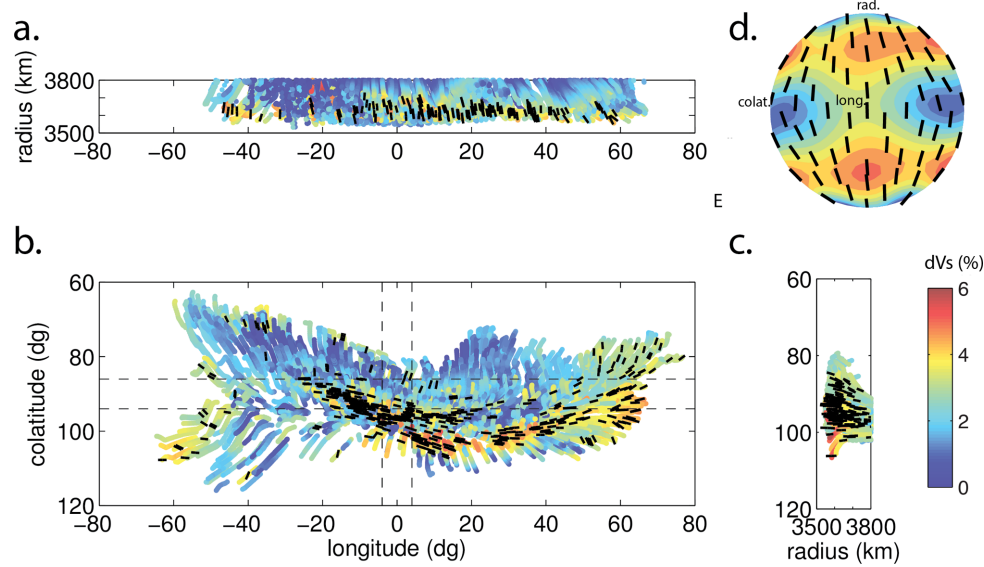


**Figure 7.** Shear wave splitting strength and fast axis direction for the model of perovskite mixed with periclase. Shear wave splitting strength is shown in colour up to 6 per cent (red) along the tracers. Samples of fast axis directions, projected on each cross-section plane, are shown in black and scaled to fast axis strength. Panels (a)–(c) show three cross-sections with splitting results for phases propagating orthogonal to these cross-sections (Fig. 4). The results are viewed (a) from the south, (b) from beneath the slab and (c) from the east (note that the projection in (c) is rotated by 90° compared to panel (a) and so are the fast axis directions). The results in (a) and (c) are slices through the model as bounded by the dashed lines in (b). Panel (b) shows the anisotropy directly above the core–mantle boundary in the horizontal plane. Panel (d) represents the shear wave splitting for one location (long. =  $-19.3^\circ$ , colat. =  $83.3^\circ$ , rad. = 3567 km) as a function of all propagation directions. The CMB is horizontal and the view is from the east.

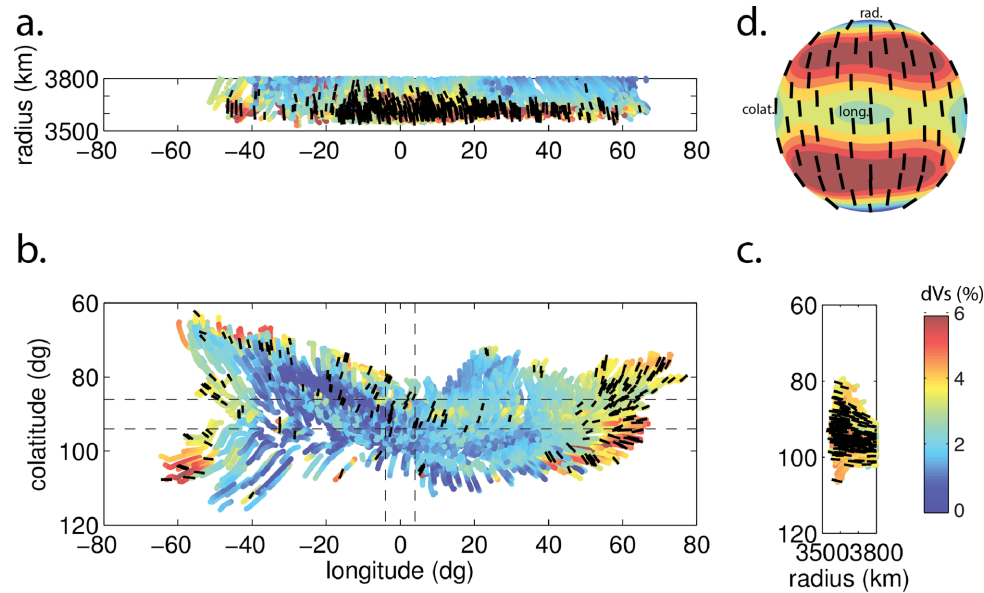


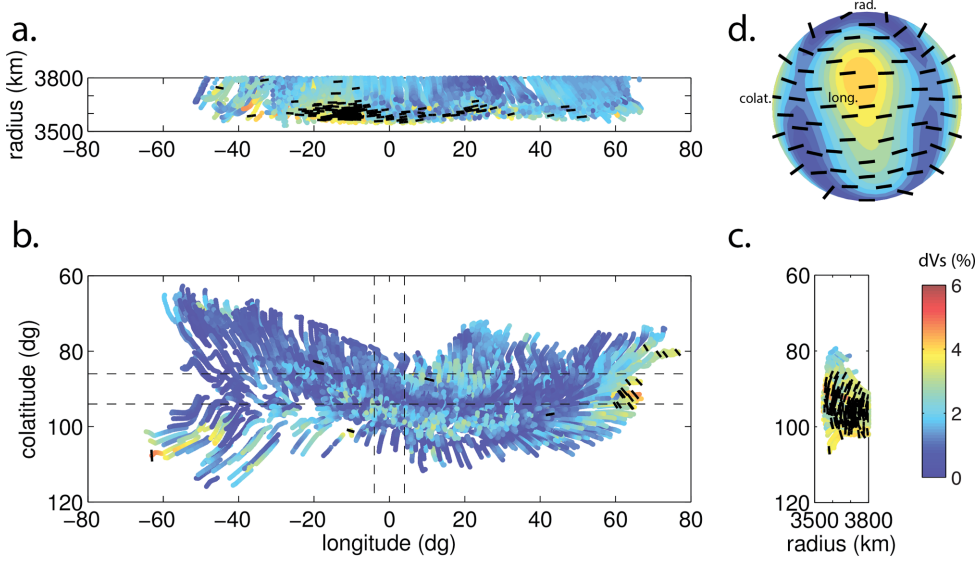
**Figure 8.** Shear wave splitting strength and fast axis direction for the model of pPv A mixed with periclase. Shear wave splitting strength is shown in colour up to 6 per cent (red) along the tracers. Samples of fast axis directions, projected on each cross-section plane, are shown in black and scaled to fast axis strength [(a) from the south, (b) from beneath the slab, (c) from the east]. Panel (d) represents the splitting for one location as a function of propagation direction. For more detail see Fig. 4 and the caption of Fig. 7.

models can account for observations of strong lateral variations in splitting. If one considers that most core phases that measure azimuthal anisotropy do not propagate purely vertically, model pPv C shows the strongest splitting for subvertical propagation paths (subplot d.).

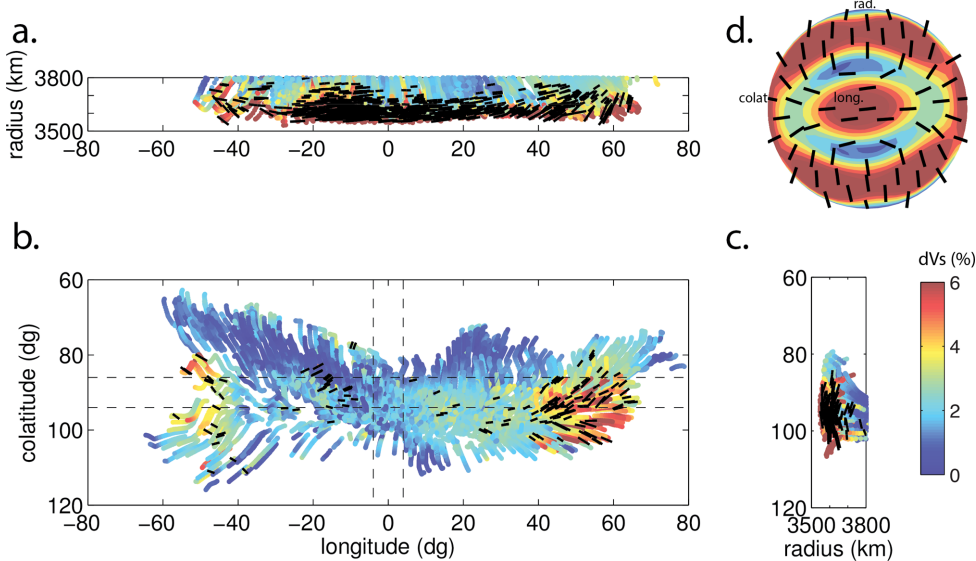
It is also interesting to look at splitting in waves that cross the slab (subplots a) compared to those that propagate parallel to the slab (subplots c). The Pv and pPv A models have faster vertically polarized waves; consistent with the radial anisotropic patterns in

Fig. 5, but inconsistent with seismic observations. For both models the fast direction varies little as a function of azimuth of the propagating phase.

Model pPv B shows consistently fast horizontally polarized waves in both directions. Model pPv B shows strong splitting for phases propagating along the slab, and only small patches of moderate splitting in the direction of subduction. This directional variation in the amount of splitting should be discernible in seismic observations to confirm this model.



**Figure 9.** Shear wave splitting strength and fast axis direction for the model of pPv B mixed with periclase. Shear wave splitting strength is shown in colour up to 6 per cent (red) along the tracers. Samples of fast axis directions, projected on each cross-section plane, are shown in black and scaled to fast axis strength [(a) from the south, (b) from beneath the slab, (c) from the east]. Panel (d) represents the splitting for one location as a function of propagation direction. For more detail see Fig. 4 and the caption of Fig. 7.



**Figure 10.** Shear wave splitting strength and fast axis direction for the model of pPv C mixed with periclase. Shear wave splitting strength is shown in colour up to 6 per cent (red) along the tracers. Samples of fast axis directions, projected on each cross-section plane, are shown in black and scaled to fast axis strength [(a) from the south, (b) from beneath the slab, (c) from the east]. Panel (d) represents the splitting for one location as a function of propagation direction. For more detail see Fig. 4 and the caption of Fig. 7.

Model pPv C shows the strongest splitting in both directions. The patches of strongest splitting are localized in the radial direction in the lowermost 100–150 km of the slab. Model pPv C also shows some rotation of fast axis at the long edges of the slab. However, for this model it would be difficult to recognize the subduction direction from orthogonal paths, due to the small differences. Slab orientations could be recognized from elongated regions of strong, deep localized anisotropy.

Observations of splitting in D'' are obviously never made from purely horizontally propagating phases; these phases always have a vertical component coming into and out of the D'' layer. From subplot d. one can infer the fast axis for a phase travelling at a

subhorizontal angle to the core–mantle boundary. Models Pv, pPv A and pPv B do not suggest much variation in fast axis direction, while the fast axis for pPv C suggests the most rotation.

## 4 DISCUSSION

### 4.1 Presence of post-perovskite

One of our goals is to exclude models of composition and deformational behaviour when the resulting anisotropic patterns contradict observations. Similar to our 2-D results (Wenk *et al.* 2011), we see

here that CPO anisotropy caused by perovskite does not fit seismic observations; the presence of post-perovskite in D'' is required. The patterns can further constrain the dominant slip system in post-perovskite. The sign of radial shear wave anisotropy beneath slab regions argues for a main slip system along (010) or (001) (pPv B or C).

Recent studies have followed a comparable approach and have argued for specific slip systems. Walker *et al.* (2011) compute CPO anisotropy in 3-D global flow models that are based on a joint inversion of isotropic shear wave velocities and other geo-physical constraints. After modelling CPO anisotropy along their tracers, they calculate correlation coefficients between their global CPO anisotropic models and global models of radial anisotropy for shear waves. Their correlation coefficients are mostly positive for post-perovskite with slip on (100) and (010) (comparable to our models pPv A and pPv B, respectively) while negative for (001)-slip (model pPv C). They mention that this correlation results from regions beneath the Pacific and Africa where  $V_{SV} > V_{SH}$  and that are related to regions of strong horizontal flow in their geodynamic model. Whether these are the regions of strong horizontal flow in the Earth remains questionable. Their flow models, similar to ours, do not contain distinctive thermochemical piles to represent the regions of low shear velocities and opposite radial anisotropy. It is unlikely that these regions represent accumulation of subducted slabs (Li & McNamara 2013). Presence of piles of distinctive material would change the convective pattern and shift the location of regions of upwelling (McNamara & Zhong 2005). As the study of Walker *et al.* (2011) also mentions, depending on the Clapeyron slope of the perovskite to post-perovskite transition, post-perovskite might not be present in these warmer regions. A recent study shows that the resulting inherited anisotropic signature in perovskite after converting back from post-perovskite would be consistent with seismic observations (Dobson *et al.* 2013). Without thermochemical piles or lateral variations in phase, a global correlation might not be appropriate. We focus our conclusions on regions of strong observed anisotropy in cold regions where subducting slabs and the presence of post-perovskite are most likely (e.g. Alaska).

## 4.2 Comparison to local seismic splitting observations

### 4.2.1 Horizontally propagating phases

A number of studies observe anisotropy in seismic phases that propagate mainly horizontally in D'', for example, S, ScS and Sdiff. The anisotropy such phases would encounter in our models is shown in panels (a) and (c) of Figs 7–10. The observational studies based on these phases conclude on horizontal or tilted fast axis directions (e.g. Cottaar & Romanowicz 2013; Nowacki *et al.* 2013) consistent with models pPv B and C. None of them find the purely vertical fast axes seen in the Pv and pPv A models. Differentiating between the pPv B and pPv C models on the basis of observations is more difficult. The following features of these models as discussed in Section 3 could further argue for either slip system:

- (i) As the models of pPv B and C show opposite signatures for radial P-wave anisotropy, observations of radial P-wave anisotropy beneath slabs could further constrain these slip systems.
- (ii) The model of pPv C is characterized by strong localized anisotropy close the CMB. Overall the anisotropy in model pPv B is weaker.

(iii) For horizontally propagating waves, model pPv B shows stronger anisotropy for phases propagating parallel to the slab than for those crossing the slab.

(iv) For vertically propagating waves (e.g. SK(K)S), model pPv C features localized patches of strong splitting.

(v) The fast axis in model pPv C shows stronger tilt from horizontal for subhorizontal propagating seismic phases than the fast axis in model pPv B.

Nowacki *et al.* (2013) present observations of crossing rays, and conclude from synthetic waveform modelling that there is a slight correlation between their observations and synthetic models for pPv B. Here we argue for pPv C in a more qualitative comparison. Their main observations beneath subducted slab regions (S1, S2, E1 and E2 in their paper) can be summarized to show purely horizontal fast axis for paths in the N–S direction, and tilted, stronger splitting in the crossing direction. It is interesting to note that the crossing direction show larger splitting times while having shorter paths in D''. The suggested geometry of the slab from their geodynamic model is N–S: roughly consistent with subduction zone at the surface. The N–S oriented measurements are thus slab parallel and suggest a purely horizontal fast axis as is seen in our pPv B and pPv C models. For the crossing rays, our pPv B model would predict weaker anisotropy; while our pPv C model suggests both stronger anisotropy and possibly a tilted fast axis. The latter is more consistent with their observations. The fact that their crossing rays have a shorter path length in D'' but still show strong anisotropy also argues for model pPv C.

The correlation found in Nowacki *et al.* (2013) is only based on fast axis angle direction and not on the amplitude of anisotropy. Their synthetic modelling, however, predicts the same pattern of stronger splitting across the slab compared to along the slab for pPv C. We do recognize the trickiness of interpreting relative anisotropic strength and small rotations in fast axis, and the inherited trade-off with the length and angle of the path through the anisotropic region. This calls for a global geodynamic model and the synthetic splitting predictions for paths corresponding to specific observations, that is the approach followed by Nowacki *et al.* (2013).

The observations of Cottaar & Romanowicz (2013) are for the Sdiff phase in one azimuthal direction south of the African LLSVP. The anisotropy here is constrained to the region where the Sdiff phases turns upwards. The ~45° fast axis found for a subhorizontal propagating phase is best explained by the pPv C model. The waveform modelling of that study shows that when the anisotropy is constrained to the lowermost 150 km, the required splitting strength is 8 per cent, similar to the splitting strengths in model pPv C here. Cottaar & Romanowicz (2013) find a strong lateral gradient in the strength of anisotropy. The correlation of the strong anisotropy with the fast isotropic velocities, highly suggests the presence of slab material in this region. The change in anisotropic strength can be related to the change from slab material to non-slab material. Although most observations of seismic anisotropy in D'' do appear to correlate with slab regions, it is important to note that our model does not rule out the presence of anisotropy (either from CPO or SPO) outside of the slab.

### 4.2.2 Vertically propagating phases

Our models show that the strongest correlation of fast axis direction with horizontal flow is at the edges of the slab, which can be seen with vertically propagating waves. Only the model for perovskite

predicts strong anisotropy with slab-parallel fast axes in the centre where flow is mostly vertical.

Long (2009) finds strong variations in lateral azimuthal anisotropy to the west of Mexico from SKS–SKKS differential splitting. Her study maps a consistent fast axis over an elongated region of tens of degrees. This elongated region, combined with predictions of palaeo-slabs, suggests an N–S oriented slab. The fast axis direction is orthogonal to the direction in which this region is elongated, which appears to suggest a general fast axis direction orthogonal to the slab. This differs from the slab-parallel direction seen at the centre in our Pv model—another argument for the presence of post-perovskite. There are small patches of weak slab-orthogonal directions at the long edge of the slab in our Pv and pPv A models. Otherwise it remains difficult to reconcile the fast axis observations with these models. Other studies of SK(K)S splitting show differential splitting around the boundaries of the African LLSVP (Wang & Wen 2007; Lynner & Long 2012, 2014) and might, similar to Cottaar & Romanowicz (2013), reflect the presence of slab material outside of the slow region.

Focusing on the pPv C model, the overall picture suggests the fast axis directions of anisotropy can be mapped into flow directions. The centre lowermost part of the slab is characterized by strong horizontal fast axis directions that are orthogonal to the vertical flow of the slab impinging on the CMB. Horizontally propagating waves show the strongest splitting in these regions. The horizontal flows at the edges of the slab, on the other hand, are best constrained by vertically propagating waves. The fast axis direction seen there is parallel to the horizontal flow direction.

While the pPv B model explains the observed signature of shear wave radial anisotropy, the weak anisotropy in this model, especially for vertically propagating phases, would give little hope of mapping flow directions.

#### 4.3 Limitations of these models

A number of assumptions and simplifications underlie this model of CPO anisotropy.

The process of a slab impinging on the CMB is simulated in a 3-D partial spherical model which allows us to increase the spatial resolution substantially, compared to a full spherical model. In order to minimize the influences from side boundary conditions, we constrained the slab to subduct at the centre of the model. In addition, the geodynamic model is iso-chemical and we focus on dynamics in subducting regions. Thermochemical piles (hypothesized to cause the LLSVPs) in upwelling regions and away from subducting regions are not considered. Furthermore, we used our best estimated physical parameters (e.g. viscosity, Rayleigh number, internal heating) of Earth's mantle to simulate the dynamics of subducting slabs. We point out that these physical parameters have uncertainty, and the variations of these parameters and their potential effects on the dynamics of subducting slabs need to be explored in further studies.

We simplify our model by not accounting for the perovskite to post-perovskite transition specifically. When this phase transition occurs texture could be inherited, as shown for the post-perovskite to perovskite transition (Dobson *et al.* 2013). Away from the transition, this inherited texture would be overridden due to the strong deformation as the slab hits the CMB. We are careful to only interpret the anisotropy patterns in the lowermost part of the slab, where post-perovskite is expected, if at all, to be present (Grocholski *et al.* 2012). The lack of the transition also withholds us from

comparing our models to observations of PdP and SdS reflection polarities (Thomas *et al.* 2011).

The presence of post-perovskite would also imply thermodynamic effects in the geodynamic model, both from the energetics of the transition (Oganov & Ono 2004) and from the change in viscosity (Ammann *et al.* 2010; Nakagawa & Tackley 2011). These effects are not accounted for in our model, but are not expected to affect the deformational regime enough to change the anisotropic signatures.

It is important to note here that our assumed composition does not reproduce the absolute isotropic velocities and density of the lowermost mantle. A large range of perovskite to periclase ratios have been proposed for the lower mantle (Javoy *et al.* 2010; Murakami *et al.* 2012), but finding a unique solution is difficult (e.g. Cobden *et al.* 2009; Cottaar *et al.* 2014). While the ratio might strongly change how the deformation is distributed amongst the weaker periclase phase and the stronger (post)perovskite phase, we still expect the (post)perovskite phase to dominate the anisotropic patterns as we see in our models here. Our composition is also simplified by only including the pure Mg end-member phases. The deformational behaviour which would result from including other major elements—Fe being the main candidate—remains uncertain. Deformation of (Fe, Mg)O shows an {001} texture (Lin *et al.* 2009). (Fe, Mg)O is intrinsically more anisotropic than pure periclase (Marquardt *et al.* 2009). Deformation results on ferrous post-perovskite have shown strong deformation on (100) (Mao *et al.* 2010), which is in agreement with our pPv A model, but is inconsistent with seismic observations. Considering the uncertainty of deformation in two phase systems and the effect of other major elements in mineral physics, we do not expect that anisotropy can add an additional constraint on the perovskite to periclase ratio and the major element composition of the lowermost mantle.

A number of assumptions cause the seismic anisotropy in our models to be stronger than observed. The synthetic shear wave radial anisotropy (Fig. 5) is about twice as strong as in global models. The inferred anisotropic strength in local observations is on the order of several percent, compared to maxima of >10 per cent in some patches in our models.

On the one hand, one can argue that the observations underestimate the actual anisotropy. Global inversion models produce damped and smoothed results. The anisotropic strength based on local observations represent an integrated effect through highly variable anisotropy and changing inclination angle. Additionally interpreted strength will trade-off with the assumed lateral and radial extent of the anisotropy. As mentioned before, the full-waveform modelling of anisotropy of Cottaar & Romanowicz (2013), with up to 8 per cent localized in the lowermost 150 km of the mantle, almost reaches the percentages seen in model pPv C.

On the other hand, our ideal scenario modelling will be overestimating the strength. Deformation is assumed in this study to be purely accommodated by dislocation creep. Including boundary diffusion mechanisms would lower the anisotropic strength. Recrystallization could further reduce the anisotropy. These mechanisms are generally not thought to affect the anisotropic patterns, although recent experiments suggest CPO from diffusion creep in olivine is possible (Miyazaki *et al.* 2013). Both the overestimation of anisotropic strength in our models and the underestimation in observations are additional arguments for the anisotropy in the pPv B model to be unrealistically weak.

To apply the proposed interpretations of geodynamic flow, better coverage of seismic anisotropy is needed. Specifically, we need azimuthal anisotropy observations, in order to map out regions of

strong horizontal flow, and crossing splitting measurements beneath impinging slabs. Currently, observations appear limited by the geometry of suitable station and earthquake coverage and the required corrections for upper mantle anisotropy, providing a future challenge for interpreting deep mantle flow and eventually constraining the validity of geodynamic models.

## 5 CONCLUSIONS

We have modelled synthetic CPO anisotropy assuming a phase composition and microscopical deformation mechanisms in a 3D geodynamic model of a slab impinging on the core–mantle boundary. The mineralogical models assume a composition consisting of perovskite and post-perovskite, as well as different main slip systems for post-perovskite, mixed with periclase. Our modelling of synthetic anisotropy results in seismically distinguishable anisotropic patterns, on which the validity of the assumed mineralogical behaviour can be tested. Overall, we find strong radial anisotropy where the slab impinges on the CMB, and strong azimuthal anisotropy in regions of horizontal flow—mainly at the short edges of the slab. As horizontally polarized shear waves are observed to be faster than vertically polarized ones in fast regions, post-perovskite with a main slip on (010) or (001) (model pPv B and C) seem plausible models to explain radial shear wave anisotropy. Post-perovskite with main slip on (010) (model pPv B), however, predicts only significant splitting along the length of the slab (slab-parallel) and not in other directions; this trend is not seen in observations. Its overall weak splitting cannot explain the persistently emerging observations of strong splitting. Our successful model of synthetic anisotropy for post-perovskite with a slip on (001) (pPv C) is a good starting point for mapping flow directions in the lowermost mantle. Using vertical propagating phases, one can link the fast axis direction of azimuthal anisotropy to the direction of horizontal flow at the edges of the slab. Strong splitting in horizontally propagating phases is interpretable as the region where the slab impinges on the CMB. One could combine this information on seismic anisotropy with that on the distribution of fast isotropic velocities and palaeo-slab predictions to map out the location of deep mantle slabs.

## ACKNOWLEDGEMENTS

Some of the calculations and figures make use of the Matlab Seismic Anisotropy Toolkit ([www1.gly.bris.ac.uk/MSAT/](http://www1.gly.bris.ac.uk/MSAT/)). This work was mainly supported by NSF/CSEDI grant 1067513, NSF EAR1343908 (HRW), and European Research Council's 'Advanced Grant' WAVETOMO. SC was partially funded by the Drapers' Company Junior Research Fellowship from Pembroke College, Cambridge. Thanks to two anonymous reviewers for their improvements to this manuscript.

## REFERENCES

- Ammann, M., Brodholt, J., Wookey, J. & Dobson, D., 2010. First-principles constraints on diffusion in lower-mantle minerals and a weak D'' layer, *Nature*, **465**, 462–465.
- Babuska, V. & Cara, M., 1991. *Seismic Anisotropy in the Earth*, Kluwer.
- Becker, T., Kustowski, B. & Ekström, G., 2008. Radial seismic anisotropy as a constraint for upper mantle rheology, *Earth planet. Sci. Lett.*, **267**(1), 213–227.
- Beghein, C., Trampert, J. & Heijst, H.V., 2006. Radial anisotropy in seismic reference models of the mantle, *J. geophys. Res.*, **111**(B2), 1–9.
- Boschi, L. & Dziewonski, A.M., 2000. Whole Earth tomography from delay times of P, PcP, and PKP phases: lateral heterogeneities in the outer core or radial anisotropy in the mantle?, *J. geophys. Res.*, **105**(B6), 13 675–13 696.
- Browaeys, J.T. & Chevrot, S., 2004. Decomposition of the elastic tensor and geophysical applications, *Geophys. J. Int.*, **159**(2), 667–678.
- Carrez, P., Ferré, D. & Cordier, P., 2007. Implications for plastic flow in the deep mantle from modelling dislocations in MgSiO<sub>3</sub> minerals., *Nature*, **446**(7131), 68–70.
- Carrez, P., Ferré, D. & Cordier, P., 2009. Peierls-Nabarro modelling of dislocations in MgO from ambient pressure to 100 GPa, *Model. Simul. Mater. Sci. Eng.*, **17**(3), 035010, doi:10.1088/0965-0393/17/3/035010.
- Catalli, K., Shim, S. & Prakapenka, V., 2009. Thickness and Clapeyron slope of the post-perovskite boundary, *Nature*, **462**(7274), 782–785.
- Chang, S.-J., Ferreira, A.M., Ritsema, J., van Heijst, H.J. & Woodhouse, J.H., 2014. Global radially anisotropic mantle structure from multiple datasets: a review, current challenges, and outlook, *Tectonophysics*, **617**, 1–19.
- Cobden, L., Goes, S., Ravenna, M., Styles, E., Cammarano, F., Gallagher, K. & Connolly, J., 2009. Thermochemical interpretation of 1D seismic data for the lower mantle: the significance of nonadiabatic thermal gradients and compositional heterogeneity, *J. geophys. Res.*, **114**, B11309, doi:10.1029/2008JB006262.
- Cordier, P., Ungár, T., Zsoldos, L. & Tichy, G., 2004. Dislocation creep in MgSiO<sub>3</sub> perovskite at conditions of the Earth's uppermost lower mantle, *Nature*, **428**(6985), 837–840.
- Cottaar, S. & Romanowicz, B., 2013. Observations of changing anisotropy across the southern margin of the African LLSVP, *Geophys. J. Int.*, **195**(2), 1184–1195.
- Cottaar, S., Heister, T., Rose, I. & Unterborn, C., 2014. Burnman – a lower mantle mineral physics toolkit, *Geochem. Geophys. Geosyst.*, **15**(4), 1164–1179.
- Dawson, P.R. & Wenk, H.-R., 2000. Texturing of the upper mantle during convection, *Phil. Mag. A*, **80**(3), 573–598.
- Devincre, B., Kubin, L., Lemarchand, C. & Madec, R., 2001. Mesoscopic simulations of plastic deformation, *Mater. Sci. Eng.: A*, **309–310**, 211–219.
- Dobson, D., Miyajima, N., Nestola, F., Alvaro, M., Casati, N., Liebske, C. & Walker, A., 2013. Strong inheritance of texture between perovskite and post-perovskite in the D'' layer, *Nat. Geosci.*, **6**, 575–578.
- Eshelby, J., 1957. The determination of the elastic field of an ellipsoidal inclusion, and related problems, *Proc. R. Soc. Lond.*, **241**(1226), 376–396.
- Ford, S., Garner, E. & McNamara, A., 2006. A strong lateral shear velocity gradient and anisotropy heterogeneity in the lowermost mantle beneath the southern Pacific, *J. geophys. Res.: Solid Earth*, **111**(B3), doi:10.1029/2004JB003574.
- Garnero, E. & Lay, T., 1997. Lateral variations in lowermost mantle shear wave anisotropy, *J. geophys. Res.*, **102**, 8121–8135.
- Garnero, E., Maupin, V., Lay, T. & Fouch, M., 2004. Variable azimuthal anisotropy in Earth's lowermost mantle, *Science*, **306**(5694), 259–261.
- Grocholski, B., Catalli, K., Shim, S. & Prakapenka, V., 2012. Mineralogical effects on the detectability of the postperovskite boundary, *Proc. Natl. Acad. Sci.*, **109**(7), 2275–2279.
- Hall, S., Kendall, J. & van der Baan, M., 2004. Some comments on the effects of lower-mantle anisotropy on SKS and SKKS phases, *Phys. Earth planet. Int.*, **146**(3–4), 469–481.
- He, X. & Long, M.D., 2011. Lowermost mantle anisotropy beneath the northwestern Pacific: evidence from PcS, ScS, SKS, and SKKS phases, *Geochem. Geophys. Geosyst.*, **12**(12), 1–21.
- Hirose, K., Nagaya, N., Merkel, S. & Ohishi, Y., 2010. Deformation of MnGeO<sub>3</sub> post-perovskite at lower mantle pressure and temperature, *Geophys. Res. Lett.*, **37**(20), L20302, doi:10.1029/2010GL044977.
- Itaya, T., Hirose, K., Kawamura, K. & Murakami, M., 2004. The elasticity of the MgSiO<sub>3</sub> post-perovskite phase in the Earth's lowermost mantle, *Nature*, **430**(6998), 442–445.
- Javoy, M., Kaminski, E., Guyot, F., Andrault, D., Sanloup, C., Moreira, M. & Jaupart, C., 2010. The chemical composition of the Earth: enstatite chondrite models, *Earth planet. Sci. Lett.*, **293**(3), 259–268.

- Karato, S., 1998a. Seismic anisotropy in the deep mantle, boundary layers and the geometry of mantle convection, *Pure appl. Geophys.*, **151**, 565–587.
- Karato, S., 1998b. Some remarks on the origin of seismic anisotropy in the D'' layer, *Earth Planet Space*, **50**, 1019–1028.
- Karato, S., Zhang, S. & Wenk, H., 1995. Superplasticity in Earth's lower mantle: Evidence from seismic anisotropy and rock physics, *Science*, **270**(5235), 458–461.
- Karato, S., Jung, H., Katayama, I. & Skemer, P., 2008. Geodynamic significance of seismic anisotropy of the upper mantle: new insights from laboratory studies, *Ann. Rev. Earth planet. Sci.*, **36**, 59–95.
- Karki, B., Wentzcovitch, R., Gironcoli, S.D. & Baroni, S., 2000. Ab initio lattice dynamics of MgSiO<sub>3</sub> perovskite at high pressure, *Phys. Rev. B*, **62**(22), doi:10.1103/PhysRevB.62.14750.
- Kawai, K. & Geller, R.R.J., 2010. The vertical flow in the lowermost mantle beneath the Pacific from inversion of seismic waveforms for anisotropic structure, *Earth planet. Sci. Lett.*, **297**(1–2), 190–198.
- Kendall, J., 2000. Seismic anisotropy in the boundary layers of the mantle, *Geophys. Monogr. Am. geophys. Un.*, **117**, 133–160.
- Kendall, J. & Silver, P., 1996. Constraints from seismic anisotropy on the nature of the lowermost mantle, *Nature*, **381**(6581), 409–412.
- Kendall, J. & Silver, P., 1998. Investigating causes of D'' anisotropy, *Geodyn. Ser.*, **28**, 97–118.
- Kustowski, B., Ekström, G. & Dziewonski, A., 2008. Anisotropic shear-wave velocity structure of the Earth's mantle: a global model, *J. geophys. Res.*, **113**(B6), B06306, doi:10.1029/2007JB005169.
- Lay, T. & Helmberger, D., 1983. The shear-wave velocity gradient at the base of the mantle, *J. geophys. Res.: Solid Earth*, **88**(B10), 8160–8170.
- Lay, T. & Young, C., 1991. Analysis of seismic SV waves in the core's penumbra, *Geophys. Res. Lett.*, **18**(8), 1373–1376.
- Lay, T., Williams, Q. & Garnero, E.J., 1998. The core–mantle boundary layer and deep Earth dynamics, *Nature*, **392**(6675), 461–468.
- Lebensohn, R. & Tomé, C., 1993. A self-consistent anisotropic approach for the simulation of plastic deformation and texture development of polycrystals: application to zirconium alloys, *Acta Metall. Mater.*, **41**(9), 2611–2624.
- Lebensohn, R., Tomé, C.N. & PonteCastañeda, P., 2007. Self-consistent modelling of the mechanical behaviour of viscoplastic polycrystals incorporating intragranular field fluctuations, *Phil. Mag.*, **87**(28), 4287–4322.
- Li, M. & McNamara, A., 2013. The difficulty for subducted oceanic crust to accumulate at the Earth's core–mantle boundary, *J. geophys. Res.*, **118**(4), 1807–1816.
- Lin, J., Wenk, H., Voltolini, M., Speziale, S., Shu, J. & Duffy, T., 2009. Deformation of lower-mantle ferropericlase (Mg, Fe)O across the electronic spin transition, *Phys. Chem. Miner.*, **36**(10), 585–592.
- Long, M. & Becker, T., 2010. Mantle dynamics and seismic anisotropy, *Earth planet. Sci. Lett.*, **297**(3), 341–354.
- Long, M., Xiao, X., Jiang, Z., Evans, B. & Karato, S., 2006. Lattice preferred orientation in deformed polycrystalline (Mg, Fe)O and implications for seismic anisotropy in D'', *Phys. Earth planet. Int.*, **156**(1), 75–88.
- Long, M.D., 2009. Complex anisotropy in D'' beneath the eastern Pacific from SKS-SKKS splitting discrepancies, *Earth planet. Sci. Lett.*, **283** (1–4), 181–189.
- Lynner, C. & Long, M., 2012. Evaluating contributions to SK(K)S splitting from lower mantle anisotropy: a case study from station DBIC, Côte D'Ivoire, *BSSA*, **102**, 1030–1040.
- Lynner, C. & Long, M., 2014. Lowermost mantle anisotropy and deformation along the boundary of the African LLSVP, *Geophys. Res. Lett.*, **41**(10), 3447–3454.
- Mainprice, D., Tommasi, A., Ferré, D., Carrez, P. & Cordier, P., 2008. Predicted glide systems and crystal preferred orientations of polycrystalline silicate Mg-perovskite at high pressure: implications for the seismic anisotropy in the lower mantle, *Earth planet. Sci. Lett.*, **271**(1–4), 135–144.
- Mao, W.L., Meng, Y. & Mao, H.-K., 2010. Elastic anisotropy of ferromagnesian post-perovskite in Earth's D'' layer, *Phys. Earth planet. Int.*, **180**(3–4), 203–208.
- Marquardt, H., Speziale, S., Reichmann, H.J., Frost, D.J., Schilling, F.R. & Garnero, E.J., 2009. Elastic shear anisotropy of ferropericlase in Earth's lower mantle, *Science (New York, N.Y.)*, **324**(5924), 224–226.
- Matzel, E., Sen, M.K. & Grand, S.P., 1996. Evidence for anisotropy in the deep mantle beneath Alaska, *Geophys. Res. Lett.*, **23**(18), 2417–2420.
- McNamara, A.K. & Zhong, S., 2005. Thermochemical structures beneath Africa and the Pacific Ocean, *Nature*, **7062**, 1136–1139.
- McNamara, A., van Keken, P. & Karato, S., 2002. Development of anisotropic structure in the Earth's lower mantle by solid-state convection, *Nature*, **416**(6678), 310–314.
- Merkel, S., Wenk, H., Shu, J., Shen, G., Gillet, P., Mao, H.K. & Hernley, R.J., 2002. Deformation of polycrystalline MgO at pressures of the lower mantle, *J. geophys. Res.*, **101**(B11), 2271, doi:10.1029/2001JB000920.
- Merkel, S., Kubo, A., Miyagi, L., Speziale, S., Duffy, T., Mao, H. & Wenk, H.-R., 2006. Plastic deformation of MgGeO<sub>3</sub> post-perovskite at lower mantle pressures, *Science*, **311**(5671), 644–646.
- Merkel, S., McNamara, A., Kubo, A. & Speziale, S., 2007. Deformation of (Mg,Fe)SiO<sub>3</sub> post-perovskite and D'' anisotropy, *Science*, **316**(5832), 1729–1732.
- Metsue, A., Carrez, P., Mainprice, D. & Cordier, P., 2009. Numerical modelling of dislocations and deformation mechanisms in CaIrO<sub>3</sub> and MgGeO<sub>3</sub> post-perovskites: comparison with MgSiO<sub>3</sub> post-perovskite, *Phys. Earth planet. Inter.*, **174**(1–4), 165–173.
- Miyagi, L., Merkel, S., Yagi, T., Sata, N., Ohishi, Y. & Wenk, H., 2009. Diamond anvil cell deformation of CaSiO<sub>3</sub> perovskite up to 49GPa, *Phys. Earth planet. Inter.*, **174**(1), 159–164.
- Miyagi, L., Kanitpanyacharoen, W. & Kærcher, P., 2010. Slip Systems in MgSiO<sub>3</sub> post-perovskite: implications for D'' Anisotropy, *Science*, **329**(5999), 1639–1641.
- Miyagi, L., Kanitpanyacharoen, W., Stackhouse, S., Militzer, B. & Wenk, H.-R., 2011. The enigma of post-perovskite anisotropy: deformation versus transformation textures, *Phys. Chem. Miner.*, **38**(9), 665–678.
- Miyajima, N. & Walte, N., 2009. Burgers vector determination in deformed perovskite and post-perovskite of CaIrO<sub>3</sub> using thickness fringes in weak-beam dark-field images, *Ultramicroscopy*, **109**(6), 683–692.
- Miyazaki, T., Sueyoshi, K. & Hiraga, T., 2013. Olivine crystals align during diffusion creep of Earth's upper mantle, *Nature*, **502**(7471), 321–326.
- Molinari, A., Canova, G. & Ahzi, S., 1987. A self consistent approach of the large deformation polycrystal viscoplasticity, *Acta Metall.*, **35**(12), 2893–2994.
- Montagner, J. & Nataf, H., 1986. A simple method for inverting the azimuthal anisotropy of surface waves, *J. geophys. Res.*, **91**(B1), 511–520.
- Murakami, M., Hirose, K., Kawamura, K., Sata, N. & Ohishi, Y., 2004. Post-perovskite phase transition in MgSiO<sub>3</sub>, *Science*, **304**(5672), 855–858.
- Murakami, M., Ohishi, Y., Hirao, N. & Hirose, K., 2012. A perovskitic lower mantle inferred from high-pressure, high-temperature sound velocity data, *Nature*, **285**(7396), 90–94.
- Nakagawa, T. & Tackley, P., 2011. Effects of low-viscosity post-perovskite on thermo-chemical mantle convection in a 3-D spherical shell, *Geophys. Res. Lett.*, **38**(4), L04305, doi:10.1029/2010GL046494.
- Nisr, C., Ribárik, G., Ungár, T., Vaughan, G.B.M., Cordier, P. & Merkel, S., 2012. High resolution three-dimensional X-ray diffraction study of dislocations in grains of MgGeO<sub>3</sub> post-perovskite at 90 GPa, *J. geophys. Res.: Solid Earth*, **117**(B3), B03201, doi:10.1029/2011JB008401.
- Niu, F. & Perez, A., 2004. Seismic anisotropy in the lower mantle: a comparison of waveform splitting of SKS and SKKS, *Geophys. Res. Lett.*, **31**(24), L24612, doi:10.1029/2004GL021196.
- Nowacki, A., Wookey, J. & Kendall, J., 2010. Deformation of the lowermost mantle from seismic anisotropy, *Nature*, **467**(7319), 1091–1094.
- Nowacki, A., Wookey, J. & Kendall, J.-M.J., 2011. New advances in using seismic anisotropy, mineral physics and geodynamics to understand deformation in the lowermost mantle, *J. Geodyn.*, **52**(3–4), 205–228.
- Nowacki, A., Walker, A., Wookey, J. & Kendall, J., 2013. Evaluating post-perovskite as a cause of D'' anisotropy in regions of palaeosubduction, *Geophys. J. Int.*, **192**(3), 1085–1090.
- Oganov, A. & Ono, S., 2004. Theoretical and experimental evidence for a post-perovskite phase of MgSiO<sub>3</sub> in Earth's D'' layer, *Nature*, **430**(6998), 445–448.

- Oganov, A.R., Martonák, R., Laio, A., Raiteri, P. & Parrinello, M., 2005. Anisotropy of Earth's D'' layer and stacking faults in the MgSiO<sub>3</sub> post-perovskite phase, *Nature*, **438**(7071), 1142–1144.
- Okada, T., Yagi, T., Niwa, K. & Kikegawa, T., 2010. Lattice-preferred orientations in post-perovskite-type MgGeO<sub>3</sub> formed by transformations from different pre-phases, *Phys. Earth planet. Inter.*, **180**(3), 195–202.
- Panning, M. & Romanowicz, B., 2006. A three-dimensional radially anisotropic model of shear velocity in the whole mantle, *Geophys. J. Int.*, **167**(1), 361–379.
- Panning, M., Lekić, V. & Romanowicz, B., 2010. Importance of crustal corrections in the development of a new global model of radial anisotropy, *J. geophys. Res.: Solid Earth*, **115**(B12), B12325, doi:10.1029/2010JB007520.
- Restivo, A. & Helffrich, G., 2006. Core-mantle boundary structure investigated using SKS and SKKS polarization anomalies, *Geophys. J. Int.*, **165**(1), 288–302.
- Rokosky, J.M., Lay, T. & Garnero, E.J., 2006. Small-scale lateral variations in azimuthally anisotropic D'' structure beneath the Cocos Plate, *Earth planet. Sci. Lett.*, **248**(1-2), 411–425.
- Russell, S., Lay, T. & Garnero, E., 1998. Seismic evidence for small-scale dynamics in the lowermost mantle at the root of the Hawaiian hotspot, *Nature*, **396**(6708), 255–258.
- Soldati, G., Boschi, L. & Piersanti, A., 2003. Outer core density heterogeneity and the discrepancy between PKP and PcP travel time observations, *Geophys. Res. Lett.*, **30**(4), 1190, doi:10.1029/2002GL016647.
- Stackhouse, S. & Brodholt, J., 2007. The high-temperature elasticity of MgSiO<sub>3</sub> post-perovskite, *Geophys. Monogr. Ser.*, **174**, 99–114.
- Stackhouse, S., Brodholt, J.P., Wookey, J., Kendall, J.-M. & Price, G.D., 2005. The effect of temperature on the seismic anisotropy of the perovskite and post-perovskite polymorphs of MgSiO<sub>3</sub>, *Earth planet. Sci. Lett.*, **230**(1-2), 1–10.
- Stretton, I., Heidelbach, F., Mackwell, S. & Langenhorst, F., 2001. Dislocation creep of magnesiowüstite (Mg<sub>0.8</sub>Fe<sub>0.2</sub>)O, *Earth planet. Sci. Lett.*, **194**(1), 229–240.
- Thomas, C., Wookey, J., Brodholt, J. & Fieseler, T., 2011. Anisotropy as cause for polarity reversals of D'' reflections, *Earth planet. Sci. Lett.*, **307**(3-4), 369–376.
- Tsuchiya, T., Tsuchiya, J., Umernote, K. & Wentzcovitch, R., 2004. Phase transition in MgSiO<sub>3</sub> perovskite in the Earth's lower mantle, *Earth planet. Sci. Lett.*, **224**(3), 241–248.
- Vinnik, L., Farra, V. & Romanowicz, B., 1989. Observational evidence for diffracted SV in the shadow of the Earth's core, *Geophys. Res. Lett.*, **16**(6), 519–522.
- Walker, A. & Wookey, J., 2012. MSAT-A new toolkit for the analysis of elastic and seismic anisotropy, *Comput. Geosci.*, **49**, 81–90.
- Walker, A.M., Carrez, P. & Cordier, P., 2010. Atomic-scale models of dislocation cores in minerals: progress and prospects, *Mineral. Mag.*, **74**(3), 381–413.
- Walker, A.M., Forte, A.M., Wookey, J., Nowacki, A. & Kendall, J.-M., 2011. Elastic anisotropy of D'' predicted from global models of mantle flow, *Geochem. Geophys. Geosyst.*, **12**(10), 1–22.
- Walte, N., Heidelbach, F., Miyajima, N., Frost, D. & Rubie, C., 2009. Transformation textures in postperovskite: understanding mantle flow in the D'' layer of the Earth, *Geophys. Res. Lett.*, **36**(4).
- Wang, Y. & Wen, L., 2007. Complex seismic anisotropy at the border of a very low velocity province at the base of the Earth's mantle, *J. geophys. Res.*, **112**(B9), 1–11.
- Wenk, H., Lonardeli, I., Pehl, J., Devine, J., Prakapenka, V., Shen, G. & Mao, H., 2004. In situ observation of texture development in olivine, ringwoodite, magnesiowüstite and silicate perovskite at high pressure, *Earth planet. Sci. Lett.*, **226**(3), 507–519.
- Wenk, H.-R., Cottaar, S., Tomé, C.N., McNamara, A. & Romanowicz, B., 2011. Deformation in the lowermost mantle: from polycrystal plasticity to seismic anisotropy, *Earth planet. Sci. Lett.*, **306**(1-2), 33–45.
- Wentzcovitch, R., 2010. Thermodynamic properties and phase relations in mantle minerals investigated by first principles quasiharmonic theory, *Rev. Miner. Geochem.*, **71**(1), 59–98.
- Wentzcovitch, R., Karki, B., Cococcioni, M. & de Gironcoli, S., 2004. Thermoelastic properties of MgSiO<sub>3</sub>-perovskite: insights on the nature of the Earth's lower mantle, *Phys. Rev. Lett.*, **92**(1), 1–4.
- Wentzcovitch, R.M., Tsuchiya, T. & Tsuchiya, J., 2006. MgSiO<sub>3</sub> postperovskite at D'' conditions., *Proc. Natl. Acad. Sci. U.S.A.*, **103**(3), 543–546.
- Wookey, J. & Kendall, J.-M., 2008. Constraints on lowermost mantle mineralogy and fabric beneath Siberia from seismic anisotropy, *Earth planet. Sci. Lett.*, **275**(1-2), 32–42.
- Yamazaki, D. & Karato, S., 2002. Fabric development in (Mg, Fe)O during large strain, shear deformation: implications for seismic anisotropy in Earth's lower mantle, *Phys. Earth planet. Int.*, **131**(3), 251–267.
- Zhong, S., 2006. Constraints on thermochemical convection of the mantle from plume heat flux, plume excess temperature, and upper mantle temperature, *J. geophys. Res.: Solid Earth*, **111**(B4), doi:10.1029/2005JB003972.